

# Reconfigurable chiral edge states in synthetic dimensions on an integrated photonic chip

Weiwei Liu,<sup>1,§</sup> Xiaolong Su,<sup>1,§</sup> Chijun Li,<sup>1,§</sup> Cheng Zeng,<sup>1,§</sup> Bing Wang,<sup>1,\*</sup> Yongjie Wang,<sup>1</sup> Yufan Ding,<sup>1</sup>  
Chengzhi Qin,<sup>1</sup> Jinsong Xia,<sup>1,†</sup> and Peixiang Lu<sup>1,2,‡</sup>

<sup>1</sup>*Wuhan National Laboratory for Optoelectronics and School of Physics, Huazhong University of Science and  
Technology, Wuhan 430074, China*

<sup>2</sup>*Hubei Key Laboratory of Optical Information and Pattern Recognition, Wuhan Institute of Technology, Wuhan  
430205, China*

\*Contact author: wangbing@hust.edu.cn, jsxia@hust.edu.cn, lupeixiang@hust.edu.cn

§These authors contributed equally to this work

**ABSTRACT.** Chiral edge state is a hallmark of topological physics, which has drawn significant attention across quantum mechanics, condensed matter and optical systems. Recently, synthetic dimensions have emerged as ideal platforms for investigating chiral edge states in multiple dimensions, overcoming the limitations of real space. In this work, we demonstrate reconfigurable chiral edge states via synthetic dimensions on an integrated photonic chip. These states are realized by coupling two frequency lattices with opposite pseudospins, which are subjected to programmable artificial gauge potential and long-range coupling within a thin-film lithium niobate microring resonator. Within this system, we are able to implement versatile strategies to observe and steer the chiral edge states, including the realization and frustration of the chiral edge states in a synthetic Hall ladder, the generation of imbalanced chiral edge currents, and the regulation of chiral behaviors as chirality, single-pseudospin enhancement, and complete suppression. This work provides a reconfigurable integrated photonic platform for simulating and steering chiral edge states in synthetic space, paving the way for the realization of high-dimensional and programmable topological photonic systems on chip.

## INTRODUCTION

Understanding the chiral edge states is an outstanding task for revealing the spin-orbit coupling in topological physics, which has gained great prominence in the contexts of topological insulators[1,2], valley-dependent optoelectronics[3,4] and topological photonics[5-7]. Experimental realizations have demonstrated that modulating the chiral edge states via external field engenders exotic topological phenomena, including topological phase transition[8,9], the non-Abelian Aharonov-Bohm effect[10], chiral zero modes[11], and chiral Landau levels[12]. Among these, topological nanophotonic systems have accelerated the study of chiral behaviors through artificial gauge field in photonic crystals[13], coupled resonators[14], metamaterials[15] and quasicrystals[16]. Despite the successful implementations, these approaches face inherent challenges in inflexibility and complex fabrication processes, which hinder the construction of a fully reconfigurable nanophotonic platform capable of controlling chiral edge states.

The concept of photonic synthetic dimensions is a crucial innovation that leverages the degrees of freedom of photons to construct independent dimensions, including frequency[17], arrival time of light pulses[18], mode[19] and orbital angular momentum[20]. This idea has garnered significant attention in fields like condensed-matter physics[21,22], topological photonics[8,19] and non-Hermitian photonics[23,24]. In particular, the synthetic frequency dimension holds promise for simulating lattice dynamics[25] and bosonic transport[26] by coupling individual frequency modes. The great tunability and programmability of this approach allow for flexible reconfiguration of the lattice, and the introduction of additional dimensions is more favorable for constructing high-dimensional systems[7,27-29]. Notably, one of the significant breakthroughs has been the realization of topological chiral edge modes in synthetic frequency and pseudospin dimensions. The implementation of controllable artificial gauge potential has led to fascinating chiral dynamics including spin-momentum locking, topological phase transition and chiral edge currents[8]. Whereas, there remains a lack of reconfigurable integrated photonic platforms for investigating the chiral edge states in synthetic dimensions, which are crucial for understanding the underlying chiral topology and for steering the edge states in practical applications.

In this work, we demonstrate reconfigurable chiral edge states on an integrated thin-film lithium niobate (TFLN) platform. Such synthetic chiral edges are created by coupling two frequency lattices with opposite pseudospins, which significantly extend the tunability of chiral behaviors through programmable artificial gauge potentials and long-range couplings. To implement this concept, we generate two trains of resonant frequency longitudinal modes within a TFLN microring resonator, using a pair of reversed travelling-wave modulations. The counterpropagating modes are coupled and modeled as a synthetic pseudospin dimension, consisting of clockwise (CW) and counterclockwise (CCW)

components. Based on this system, we develop versatile strategies to steer the chiral edge states on chip. First, we synthesize a chiral Hall ladder in frequency and pseudospin dimensions, and demonstrate frustration of the chiral edge currents by long-range coupling. We then create a synthetic misaligned interface by imposing additional coupling on the Hall ladder, realizing imbalanced chiral edge currents. Finally, we construct a coupled Hall ladder model by introducing next-nearest-neighbor coupling, showing that the chiral behaviors can be steered as chirality, single-pseudospin enhancement and complete suppression by controlling the artificial gauge potential.

## RESULTS

**Device design and theoretical model.** The system depicted in Figure 1(a) consists of a microring structure that supports a series of resonant frequency longitudinal modes in both clockwise (CW) and counterclockwise (CCW) directions[30]. To couple individual longitudinal modes, a pair of reversed traveling-wave modulations are introduced into the system and driven at a frequency that is an integer multiple of the free spectral range (FSR) of the microring[31]. Notably, the wavevector-matching principle permits independent modulation of optical fields in opposite propagation directions[32,33]. This configuration enables modeling of the system as two synthetic frequency lattices with reversed pseudospin degrees of freedom. Furthermore, a part of the microring waveguide is brought closer to each other, thus introducing coupling between the two pseudospins[33]. As a consequence, we realize a synthetic two-dimensional (2D) lattice resembling a series of reconfigurable frequency edges, as shown in Fig. 1(b).

To implement the concept of reconfigurable frequency edges in synthetic dimensions, we fabricate the device on a thin-film lithium niobate (TFLN) platform (see Supplemental Material for details[33]), for the advantageous electro-optic property. More recently, the advancements in integrated TFLN electro-optic modulator have significantly promoted the modulation efficiency and bandwidth[34], generating considerable interest in applications such as integrated microcomb[35], optical parametric oscillator[36], and microwave photonic engine[37]. Fig. 1(c) presents a microscopic image of the fabricated device. The transmission spectrum of the passive cavity (Fig. 1(d)) reveals that the microring cavity exhibits a high quality factor of  $3.5 \times 10^5$  and an FSR of approximately 9.34 GHz. The coupling strength ( $K$ ) between the two pseudospins is designed to be 1/10 of the FSR, resulting in a resonant peak splitting of  $2K = 1.82$  GHz in the transmission spectrum (Fig. 1(e)).

Under traveling-wave modulation, the system can be described with a tight-binding Hamiltonian[33]

$$H = - \sum_{m,s} \left[ \omega_m a_{m,s}^\dagger a_{m,s} + \sum_{l=1}^{\infty} (J_s(t) a_{m,s}^\dagger a_{m-l,s} + H.c.) \right], \quad (1)$$

$$- K \sum_m (a_{m,\uparrow}^\dagger a_{m,\downarrow} + H.c.)$$

where  $a_{m,s}$  and  $a_{m,s}^\dagger$  are the annihilation and production operators for the  $m$ -order frequency ( $m\Omega_R$ ) longitudinal mode of the cavity, with pseudospin  $s \in \{\uparrow(\text{CW}), \downarrow(\text{CCW})\}$ .  $\Omega_R/2\pi$  denotes the FSR of the microring cavity.  $J_\uparrow(t)$  and  $J_\downarrow(t)$  represent the coupling strengths along the frequency dimension, which are related to the traveling-wave modulation. For simplicity, the coupling strengths are assumed to be independent of the longitudinal mode index[30].  $K$  represents the effective coupling strength between CW and CCW pseudospin modes. To obtain a time-independent Hamiltonian, we transform to the interaction picture by defining  $\tilde{a}_{m,s} = a_{m,s} e^{-im\Omega_R t}$ . Then by applying the rotating-wave

approximation and utilizing the Fourier transform  $\tilde{a}_{k,\uparrow} = \sqrt{\frac{\Omega_R}{2\pi}} \sum_m e^{im\Omega_R k} \tilde{a}_{m,\uparrow}$ , the Hamiltonian can be written in

the quasi-momentum space ( $k$ -space) as  $H = \sum_k \tilde{\mathbf{a}}_k^\dagger \mathcal{H}(k) \tilde{\mathbf{a}}_k$ , where[33]

$$\mathcal{H}(k) = - \begin{bmatrix} \sum_{l=1}^{\infty} J_{\uparrow,l} \cos(l\Omega_R k + \varphi_{\uparrow,l}) & K \\ K & \sum_{l=1}^{\infty} J_{\downarrow,l} \cos(l\Omega_R k + \varphi_{\downarrow,l}) \end{bmatrix}. \quad (2)$$

$J_{s,l}$  is the  $l$ -order frequency components of  $J_s(t)$ , i.e.  $J_s(t) = \sum_l J_{s,l} \cos(l\Omega_R t + \varphi_{s,l})$ .  $\mathcal{H}(k)$  can be actually mapped onto a spin-orbit coupling (SOC) system[8] by rewriting as  $\mathcal{H}(k) = -\varepsilon(k) \cdot \mathbf{I} - \mathbf{B}_{\text{soc}} \cdot \boldsymbol{\sigma}$ , where  $\varepsilon(k) = [\sum_l J_{\uparrow,l} \cos(l\Omega_R k + \varphi_{\uparrow,l}) + \sum_l J_{\downarrow,l} \cos(l\Omega_R k + \varphi_{\downarrow,l})]/2$ ,  $\mathbf{B}_{\text{soc}} = \{K, 0, [\sum_l J_{\uparrow,l} \cos(l\Omega_R k + \varphi_{\uparrow,l}) - \sum_l J_{\downarrow,l} \cos(l\Omega_R k + \varphi_{\downarrow,l})]/2\}$ , and  $\boldsymbol{\sigma} = [\sigma_x, \sigma_y, \sigma_z]$  denoting the Pauli matrix, with the two pseudo-spins representing the legs of the ladders. Specifically, the eigenvalues of  $\mathcal{H}(k)$  correspond to the energy band in quasi-momentum space. The energy bands can be directly measured using time-resolved band structure spectroscopy[30,33]. Equation (2) suggests that the synthetic frequency lattices and

corresponding energy bands are governed by the modulation signals. Therefore, through controlling the modulation signals, reconfigurable edge states can be conveniently constructed to investigate the chiral features.

**Synthesizing chiral Hall ladder in frequency and pseudospin dimensions.** The Hall ladder is one of the most important physical models for studying topological edge states, which has been instrumental for realizing topological chiral edge modes of a 2D quantum Hall insulator described by the Harper-Hofstadter Hamiltonian[8,9]. In the synthetic frequency dimension, the Hall ladder is constructed by defining the modulation (coupling) terms as  $J_{\uparrow}(t)=J\cos(\Omega_R t-\varphi_0/2)$  and  $J_{\downarrow}(t)=J\cos(\Omega_R t+\varphi_0/2)$  (Figures 2(a) and 2(b)), which induce coupling between the frequency lattices corresponding to the two pseudospins respectively.  $\varphi_0$  denotes the phase contrast between the two modulation signals. It introduces an artificial gauge potential for photons, and can be interpreted as an effective magnetic flux through the ladder[17].

Fig. 2(c) illustrates the energy band of the synthetic Hall ladder, calculated using Equation (2). The color shading indicates the proportion of CW pseudospin modes. For experimental measurements, the energy band was mapped by monitoring transmission under varying laser detunings[33]. The measured energy bands (Fig. 2(d)) closely match the theoretical results. In the lower band, the CW (CCW) modes predominantly occupy positive (negative)  $k$ -states in quasi-momentum space, demonstrating the typical behavior of spin-momentum locking in the Hall ladder. Under an effective magnetic flux, photons in the legs of the ladder tend to propagate in opposite directions, resulting in the chiral edge current. The chiral current is defined as  $j_C=\sum_{m>m_0}P(m)-\sum_{m<m_0}P(m)$ [8], where  $m_0$  represents the index of the ring resonance closest to the input laser frequency.  $P(m)$  is optical power at frequency  $m\Omega_R$ , extracted from the measured optical spectra (Fig. 2(e)). The measured chiral current and its corresponding fitting using temporal coupled-mode theory (CMT) are presented in Fig. 2(f). In the lower energy band, the chiral current for the CW pseudospin is positive, indicating that photons preferentially evolve to higher frequencies. Conversely, in the higher energy band photons tend to evolve toward lower frequencies, which represents a hallmark of the photonic chiral edge current.

Specifically, the flexibility of the synthetic frequency lattice enables independent control of the lattice constants for the two legs of the Hall ladder. As an extension, long-range coupling can be introduced into one leg of the Hall ladder by defining the modulation as  $J_{\uparrow}(t)=J\cos(\Omega_R t)$  and  $J_{\downarrow}(t)=J\cos(N\Omega_R t+\varphi_0)$  ( $N=2, 3, 4, 5\dots 10$ ). This configuration creates a synthetic hetero-bilayer interface in frequency dimension. In this scenario, the edge currents exhibit a significant overall decrease, indicating a frustration of the edge currents by long-range coupling (See Supplemental Materials for details[33]).

**Imbalanced chiral edge currents in synthetic misaligned interface.** Chirality imbalance has become a compelling topic in topological physics, which has been realized through symmetry breaking in photonic metamaterials and fermionic systems[38,39]. Here, we demonstrate the emergence of imbalanced chiral edge currents by imposing an additional coupling to one pseudospin of the system. Specifically, the modulation signals are adopted as  $J_{\uparrow}(t)=J_1\cos(\Omega_R t+\varphi_1)+J_2\cos(2\Omega_R t+\varphi_2)$ , and  $J_{\downarrow}(t)=J_2\cos(2\Omega_R t+\varphi_3)$  (Figure 3(a)). This configuration gives rise to a misaligned interface composed of two sub-Hall ladders and a triangular ladder, as illustrated in Fig. 3(b). Due to the asymmetric modulations, the symmetry between the two frequency chains corresponding to different pseudospins is broken, thereby leading to the formation of imbalanced chiral edge currents.

To explore the chiral features of the synthetic misaligned interface with symmetry breaking, an effective magnetic flux is applied to the sub-Hall ladders, with phases defined as  $\varphi_3=-0.7\pi$ ,  $\varphi_1=\varphi_2=0$ . The calculated and measured energy bands of the misaligned interface are shown in Fig. 3(c) and Fig. 3(d), respectively. The energy bands retain the characteristic chiral features of the Hall ladder, as indicated by the dashed box. However, the introduction of triangular ladder through nearest-neighbor coupling leads to a deformation of the energy band structure. Consequently, the group velocity of the CCW-dominant state becomes larger than that of the CW-dominant state in the upper band, thereby supporting the imbalanced chiral edge currents in the synthetic misaligned interface. To validate the prediction, we measure the output spectra and chiral current of the synthetic misaligned interface, as shown in Figs. 3(e)-3(f). One can observe that, for the lower energy band, the chiral current for the CW pseudospin is enhanced relative to the CCW pseudospin. However, in the upper band, the chiral current for the CCW pseudospin is enhanced instead, indicating a net imbalance between the lower-moving (upper-moving) modes for CW (CCW) pseudospins within the misaligned interface. Furthermore, reversing the direction of the effective magnetic flux inverts the current direction on both legs, while maintaining the imbalanced chiral edge current characteristic[33].

**Steering chiral edge states in coupled Hall ladders.** Through introducing the next-nearest-neighbor coupling into the Hall ladder, we construct a pseudo-three-dimensional (pseudo-3D) frequency lattice. Concretely, the modulation signals are defined as  $J_{\uparrow,\downarrow}(t)=J_a\cos(\Omega_R t+\varphi_{1,2})+J_b\cos(2\Omega_R t+\varphi_{1,2})$ , where the effective magnetic fluxes in the ladders depend on the initial phase contrasts of these signals. Correspondingly, this configuration results in two Hall ladders with lattice constants of  $\Omega_R$  and  $2\Omega_R$  respectively, along with a triangular ladder formed on each leg. These sub-ladders constitute a coupled Hall ladder, as illustrated in Figure 4(a). Specifically, there are four effective magnetic fluxes in the coupled Hall ladder, including those associated with the Hall ladders having lattice constant of  $\Omega_R$  (denoted  $\theta_1$ )

and  $2\Omega_R$  (denoted  $\theta_2$ ), as well as those corresponding to the triangular ladder in the CCW (denoted  $\theta_3$ ) and CW direction (denoted  $\theta_4$ ). These fluxes are related to the modulation signals by  $\theta_1 = \varphi_2 - \varphi_1$ ,  $\theta_2 = \phi_1 - \phi_2$ ,  $\theta_3 = \phi_2 - 2\varphi_2$  and  $\theta_4 = 2\varphi_1 - \phi_1$ . By configuring these magnetic fluxes in the sub-ladders, the chiral edge states of the coupled Hall ladder can be conveniently manipulated, enabling control over chirality, chiral triviality, single-pseudospin enhancement and complete suppression. These diverse chiral edge states are summarized in a phase diagram in Fig. 4(b), where  $X = \text{sgn}(\theta_2) - \text{sgn}(\theta_1)$  and  $Y = \text{sgn}(\theta_3) - \text{sgn}(\theta_4)$ .

In the first case, we apply effective magnetic fluxes in the same direction in both Hall ladders. The initial phases of the signals are set as  $\varphi_1 = -\varphi_2 = -0.15\pi$ ,  $\phi_1 = -\phi_2 = -0.3\pi$ . Under these conditions, the energy bands are similar with that of the Hall ladder, as shown in Fig. 4(c). Consequently, the edge currents exhibit chiral behavior, with opposite directions for the upper and lower bands in the CW pseudospin modes (Figs. 4(d) and 4(e)). Based on the first case, we introduce an additional effective magnetic flux into the triangular ladders with the initial phases setting as  $\varphi_1 = \phi_2 = 0$ ,  $\phi_1 = -2\varphi_2 = 0.3\pi$ . This will impose a further influence on the chiral edge currents. Specifically, the Hall ladders produce opposite chiral edge currents in the two legs, while the triangular ladders generate chiral edge currents in the same direction. Their combined influence suppresses the chiral edge current in one leg, leading to the enhancement of the chiral edge current in the upper (lower) energy band for CW (CCW) pseudospin modes. This single-pseudospin enhancement effect is demonstrated by the energy band and edge current results shown in Figs. 4(f)-4(h). In the third case, the effective magnetic fluxes of the two Hall ladders are set in opposite directions ( $\varphi_1 = \phi_2 = 0$ ,  $\phi_1 = \varphi_2 = 0.3\pi$ ). The edge currents generated by the two coupled Hall ladders cancel each other out, resulting in a complete suppression of the chiral edge currents, as shown in Figs. 4(i)-4(k). Additionally, in the situation of  $|X| < |Y|$ , the effective magnetic fluxes in the two triangular ladders align in the same direction, while the fluxes in the two Hall ladders cancel out in opposite directions. As a consequence, the two pseudo-spin occupations become nearly identical, indicating the dissolution of the edge states and corresponds to chiral triviality.

## DISCUSSION and CONCLUSIONS

We present an integrated photonic platform for simulating chiral edge states in independent frequency and pseudospin dimensions. While the observation of chiral edge states has been explored in some other synthetic systems, such as fiber loops[8] and cold atoms[9], our platform offers several unique advantages. Firstly, such a system enables the realization of two synthetic physical dimensions within a single integrated photonic chip, which significantly reduces size and increases compactness compared to previous implementations. Secondly, this system allows for the introduction of an effective gauge potential via the controllable phase contrast between modulation signals. This approach provides more convenience and flexibility than previous systems that relied on optical path difference. Additionally, the system can accommodate various long-range couplings between the synthetic lattices, providing further regulation over the chiral edge states, even with complex modulation signals[33]. Thirdly, the nonreciprocity of the traveling-wave modulation facilitates independent modulation of the two pseudospin modes, which presents a critical feature for constructing the synthetic chiral edge states. Besides, the exceptional tunability and programmability of this platform will motivate further investigations into implementation a variety of topological effects in integrated photonics, such as the non-Hermitian chiral physics[23], Weyl semimetals[24], Floquet topological physics[40] and quantum correlations[41].

In conclusion, we have demonstrated reconfigurable chiral edge states via photonic synthetic dimensions on an integrated TFLN platform. These synthetic chiral edge states are created by coupling two frequency lattices with opposite pseudospins, which can be flexibly controlled through programmable artificial gauge potentials and long-range couplings. Within this system, we have configured versatile chiral edge states to explore and manipulate chiral behaviors, including the realization and frustration of chiral edge states in a synthetic Hall ladder, the generation of imbalanced chiral currents, and the regulation of various chiral phenomena such as chirality, single-pseudospin enhancement, and complete suppression. This work establishes a reconfigurable integrated photonic platform to simulate and steer chiral edge states in synthetic space, which opens up new avenues for the realization of high-dimensional, programmable topological photonic system on chip.

## ACKNOWLEDGMENTS

We thank Prof. Chi Zhang for the support in real-time oscilloscope measurements. The work is supported by the National Natural Science Foundation of China (No. 12374305, No. 62375097, No. 12021004). The authors gratefully acknowledged the Center of Micro-Fabrication and Characterization (CMFC) of Wuhan National Laboratory for Optoelectronics (WNLO) for their support in the nanofabrication of devices.

## REFERENCES

- [1] B. A. Bernevig and S.-C. Zhang, *Phys. Rev. Lett.* **96**, 106802 (2006).
- [2] S. Howard, L. Jiao, Z. Wang, N. Morali, R. Batabyal, P. Kumar-Nag, N. Avraham, H. Beidenkopf, P. Vir, E. Liu, C. Shekhar, C. Felser, T. Hughes, and V. Madhavan, *Nat. Commun.* **12**, 4269 (2021).
- [3] L. Ju, Z. Shi, N. Nair, Y. Lv, C. Jin, J. Velasco, C. Ojeda-Aristizabal, H. A. Bechtel, M. C. Martin, A. Zettl, J. Analytis, and F. Wang, *Nature* **520**, 650 (2015).
- [4] G.-J. Tang, X.-D. Chen, L. Sun, C.-H. Guo, M.-Y. Li, Z.-T. Tian, H.-H. Chen, H.-W. Wang, Q.-Y. Sun, Y.-D. Pan, X.-T. He, Y.-K. Su, and J.-W. Dong, *Light: Sci. Appl.* **13**, 166 (2024).
- [5] A. B. Khanikaev and G. Shvets, *Nat. Photonics* **11**, 763 (2017).
- [6] R. Barczyk, L. Kuipers, and E. Verhagen, *Nat. Photonics* **18**, 574 (2024).
- [7] N. Parappurath, F. Alpegiani, L. Kuipers, and E. Verhagen, *Sci. Adv.* **6**, aww4137 (2020).
- [8] A. Dutt, Q. Lin, L. Yuan, M. Minkov, M. Xiao, and S. Fan, *Science* **367**, 59 (2020).
- [9] M. Atala, M. Aidelsburger, M. Lohse, J. T. Barreiro, B. Paredes, and I. Bloch, *Nat. Phys.* **10**, 588 (2014).
- [10] Q. Liang, Z. Dong, J.-S. Pan, H. Wang, H. Li, Z. Yang, W. Yi, and B. Yan, *Nat. Phys.* **20**, 1738 (2024).
- [11] H. Jia, R. Zhang, W. Gao, Q. Guo, B. Yang, J. Hu, Y. Bi, Y. Xiang, C. Liu, and S. Zhang, *Science* **363**, 148 (2019).
- [12] H. Jia, M. Wang, S. Ma, R.-Y. Zhang, J. Hu, D. Wang, and C. T. Chan, *Light: Sci. Appl.* **12**, 165 (2023).
- [13] A. B. Khanikaev, S. Hossein Mousavi, W.-K. Tse, M. Kargarian, A. H. MacDonald, and G. Shvets, *Nat. Mater.* **12**, 233 (2012).
- [14] M. Hafezi, S. Mittal, J. Fan, A. Migdall, and J. M. Taylor, *Nat. Photonics* **7**, 1001 (2013).
- [15] F. Allein, A. Anastasiadis, R. Chaunsali, I. Frankel, N. Boechler, F. K. Diakonov, and G. Theocharis, *Nat. Commun.* **14**, 6633 (2023).
- [16] Y. Zhang, Z. Lan, L. Hu, Y. Shu, X. Yuan, P. Guo, X. Peng, W. Chen, and J. Li, *Opt. Lett.* **48**, 2229 (2023).
- [17] C. Qin, F. Zhou, Y. Peng, D. Sounas, X. Zhu, B. Wang, J. Dong, X. Zhang, A. Alù, and P. Lu, *Phys. Rev. Lett.* **120**, 133901 (2018).
- [18] X. Hu, S. Wang, C. Qin, C. Liu, L. Zhao, Y. Li, H. Ye, W. Liu, S. Longhi, P. Lu, and B. Wang, *Adv. Photon.* **6**, 046001 (2024).
- [19] E. Lustig, S. Weimann, Y. Plotnik, Y. Lumer, M. A. Bandres, A. Szameit, and M. Segev, *Nature* **567**, 356 (2019).
- [20] X.-W. Luo, X. Zhou, J.-S. Xu, C.-F. Li, G.-C. Guo, C. Zhang, and Z.-W. Zhou, *Nat. Commun.* **8**, 16097 (2017).
- [21] T. Ozawa and H. M. Price, *Nat. Rev. Phys.* **1**, 349 (2019).
- [22] L. Du, Y. Zhang, J.-H. Wu, A. F. Kockum, and Y. Li, *Phys. Rev. Lett.* **128**, 223602 (2022).
- [23] K. W. A. D. S. Fan, *Science* **371**, 1240 (2021).
- [24] W. Song, S. Wu, C. Chen, Y. Chen, C. Huang, L. Yuan, S. Zhu, and T. Li, *Phys. Rev. Lett.* **130**, 043803 (2023).
- [25] L. Yuan, Q. Lin, M. Xiao, and S. Fan, *Optica* **5**, 1936 (2018).
- [26] A. Senanian, L. G. Wright, P. F. Wade, H. K. Doyle, and P. L. McMahon, *Nat. Phys.* **19**, 1333 (2023).
- [27] J. Suh, G. Kim, H. Park, S. Fan, N. Park, and S. Yu, *Phys. Rev. Lett.* **132**, 033803 (2024).
- [28] L. Yuan, Q. Lin, A. Zhang, M. Xiao, X. Chen, and S. Fan, *Phys. Rev. Lett.* **122**, 083903 (2019).
- [29] D. Cheng, E. Lustig, K. Wang, and S. Fan, *Light: Sci. Appl.* **12**, 158 (2023).
- [30] A. Dutt, M. Minkov, Q. Lin, L. Yuan, D. A. B. Miller, and S. Fan, *Nat. Commun.* **10**, 3122 (2019).
- [31] L. Yuan, Y. Shi, and S. Fan, *Opt. Lett.* **41**, 741 (2016).
- [32] M. Yu, R. Cheng, C. Reimer, L. He, K. Luke, E. Puma, L. Shao, A. Shams-Ansari, X. Ren, H. R. Grant, L. Johansson, M. Zhang, and M. Lončar, *Nat. Photonics* **17**, 666 (2023).
- [33] See Supplemental Material at <http://xxxxxx>.
- [34] A. Boes, L. Chang, C. Langrock, M. Yu, M. Zhang, Q. Lin, M. Lončar, M. Fejer, J. Bowers, and A. Mitchell, *Science* **379**, eabj4396 (2023).
- [35] M. Zhang, B. Buscaino, C. Wang, A. Shams-Ansari, C. Reimer, R. Zhu, J. M. Kahn, and M. Lončar, *Nature* **568**, 373 (2019).
- [36] H. S. Stokowski, D. J. Dean, A. Y. Hwang, T. Park, O. T. Celik, T. P. McKenna, M. Jankowski, C. Langrock, V. Ansari, M. M. Fejer, and A. H. Safavi-Naeini, *Nature* **627**, 95 (2024).
- [37] H. Feng, T. Ge, X. Guo, B. Wang, Y. Zhang, Z. Chen, S. Zhu, K. Zhang, W. Sun, C. Huang, Y. Yuan, and C. Wang, *Nature* **627**, 80 (2024).
- [38] Q. Li, D. E. Kharzeev, C. Zhang, Y. Huang, I. Pletikosić, A. V. Fedorov, R. D. Zhong, J. A. Schneeloch, G. D. Gu, and T. Valla, *Nat. Phys.* **12**, 550 (2016).
- [39] X. Zhou, S. Li, C. Hu, G. Wang, and B. Hou, *Appl. Phys. Lett.* **123**, 111702 (2023).
- [40] S. K. Sridhar, S. Ghosh, D. Srinivasan, A. R. Miller, and A. Dutt, *Nat. Phys.* **20**, 843 (2024).
- [41] U. A. Javid, R. Lopez-Rios, J. Ling, A. Graf, J. Staffa, and Q. Lin, *Nat. Photonics* **17**, 883 (2023).

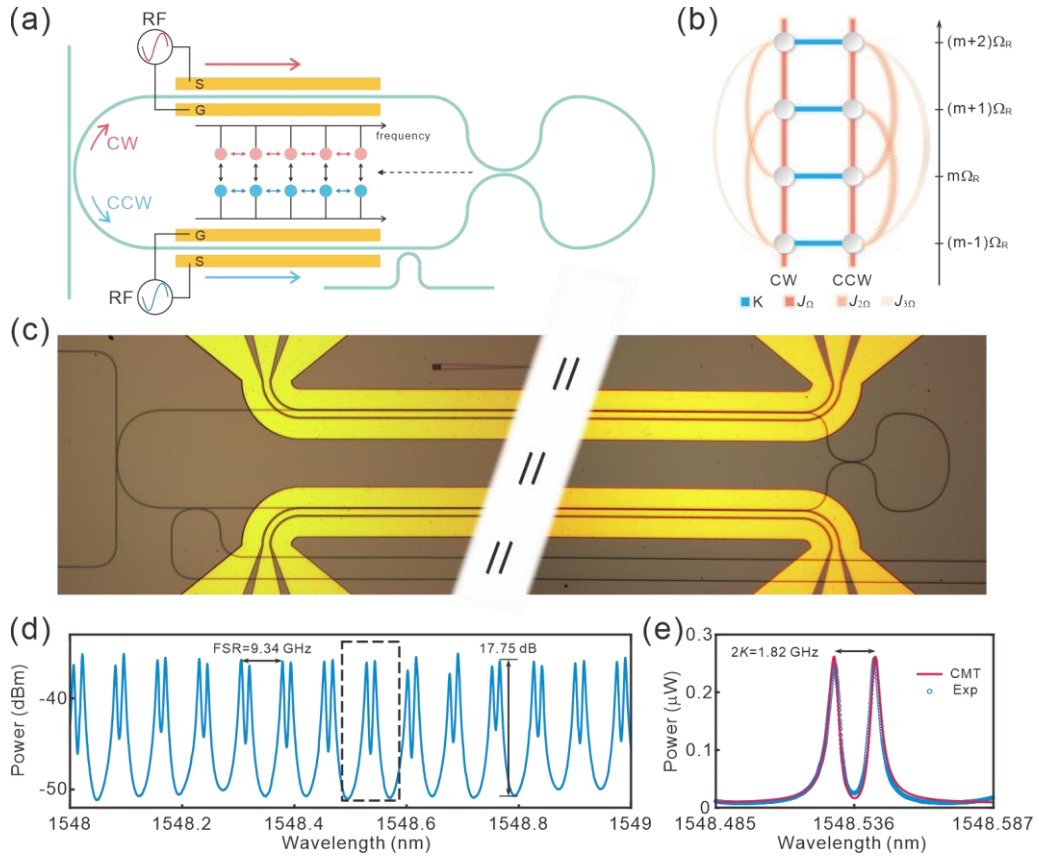


**Fig. 1. Concept of reconfigurable chiral edge states via synthetic dimensions in an integrated photonic platform.** (a) Structural schematic for realizing synthetic frequency and pseudospin dimensions in a coupled microring resonator. (b) Diagram for creating reconfigurable chiral edge states. The CW and CCW pseudospins represent the two legs of the ladder, with each leg generated by frequency longitudinal modes in the microring resonator. (c) Microscopic image of a device fabricated on TFLN platform. (d) Experimentally measured transmission spectrum of the passive cavity device. (e) An enlarged image of the transmission spectrum, which indicates a resonant peak splitting of  $2K = 1.82$  GHz.

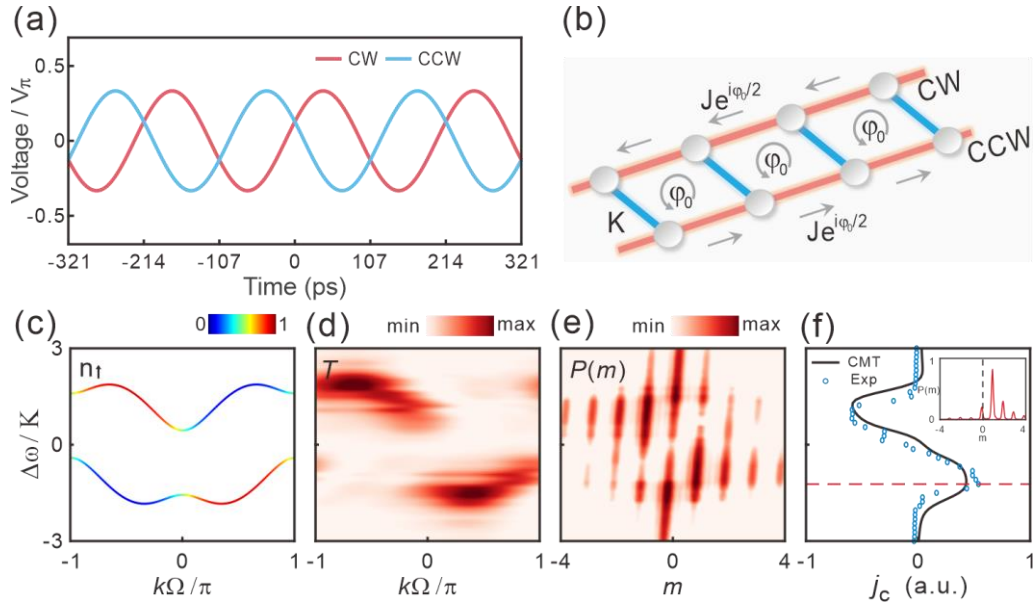


**Fig. 2. Chiral edge states in a synthetic Hall ladder.** (a) Plots of modulation signals. (b) Illustration of the corresponding model of a synthetic Hall ladder. (c) Theoretically calculated and (d) experimentally time-resolved energy band structures. (e) Experimentally measured spectra mapped with laser detunings ( $\Delta\omega$ ). (f) Chiral edge current extracted from the optical spectra, and the corresponding theoretical fittings.

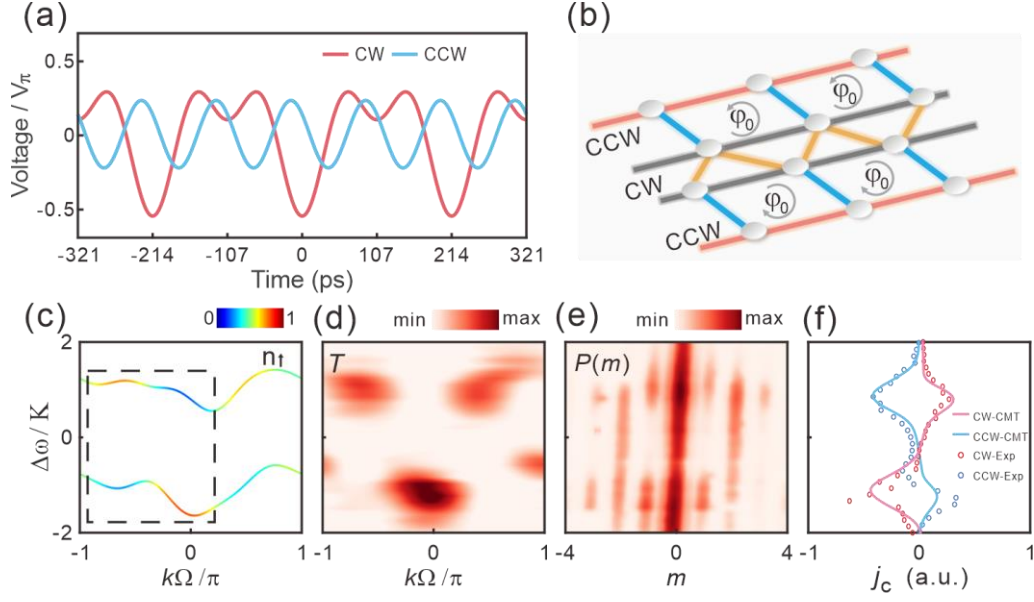


**Fig. 3. Observation of imbalanced chiral edge currents.** (a) Plots of modulation signals. (b) Illustration of the corresponding model of a synthetic misaligned interface. (c) Theoretically calculated and (d) experimentally time-resolved energy band structures. (e) Experimentally measured spectra mapped with laser detunings ( $\Delta\omega$ ). (f) Chiral edge current extracted from the optical spectra, and the corresponding theoretical fittings. The chiral current exhibits a net imbalanced distribution between the CW and CCW pseudospins.



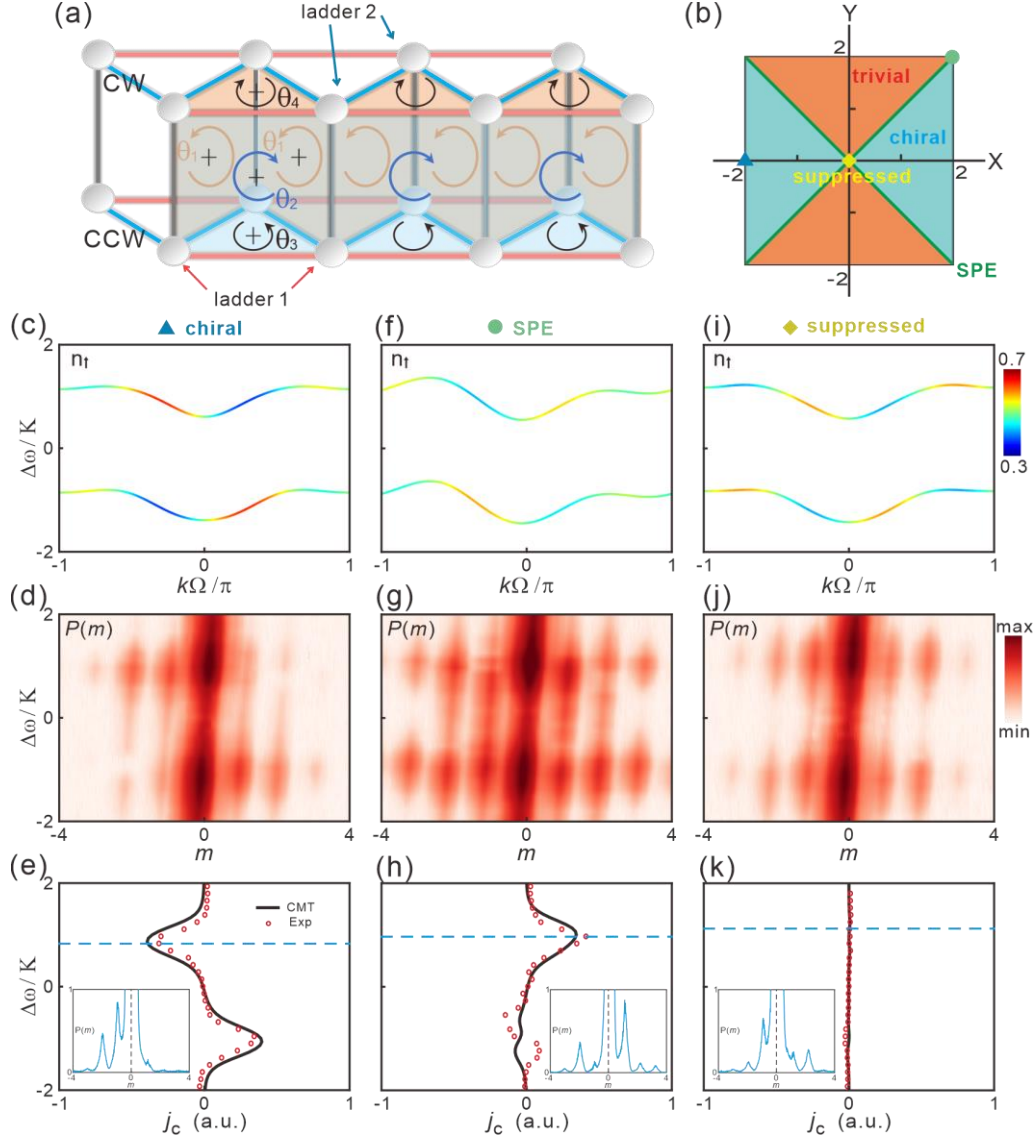


**Fig. 4. Steering chiral edge states in coupled Hall ladders.** (a) Illustration of the model of coupled Hall ladders. Four effective magnetic fluxes are defined in the coupled Hall ladder.  $\theta_1$  and  $\theta_2$  represent effective magnetic fluxes of the Hall ladders with lattice constant of FSR and twice of FSR, and  $\theta_3$  and  $\theta_4$  represent effective magnetic fluxes of the triangular ladder in CCW and CW directions. (b) Phase diagram of the chiral edge current which indicates versatile chiral edge states of chirality, chiral triviality, single-pseudospin enhancement (SPE) and complete suppression.  $X = \text{sgn}(\theta_2) - \text{sgn}(\theta_1)$  and  $Y = \text{sgn}(\theta_3) - \text{sgn}(\theta_4)$ . Calculated energy band structures, experimentally measured spectra mappings and chiral edge current for cases of (c-e) chirality, (f-h) single-pseudospin enhancement (SPE), and (i-k) complete suppression.